POROUS METALS: FROM NANO TO MACRO

Temperature-dependent mechanical behavior of three-dimensionally ordered macroporous tungsten

Kevin M. Schmalbach^{1,c)}, Zhao Wang^{2,c)}, R. Lee Penn², David Poerschke¹, Antonia Antoniou³, Andreas Stein^{2,a)}, Nathan A. Mara^{1,b)}

Received: 8 March 2020; accepted: 11 May 2020

Porous metals represent a class of materials where the interplay of ligament length, width, node structure, and local geometry/curvature offers a rich parameter space for the study of critical length scales on mechanical behavior. Colloidal crystal templating of three-dimensionally ordered macroporous (3DOM, i.e., inverse opal) tungsten provides a unique structure to investigate the mechanical behavior at small length scales across the brittle–ductile transition. Micropillar compression tests show failure at 50 MPa contact pressure at 30 °C, implying a ligament yield strength of approximately 6.1 GPa for a structure with 5% relative density. *In situ* SEM frustum indentation tests with in-plane strain maps perpendicular to loading indicate local compressive strains of approximately 2% at failure at 30 °C. Increased sustained contact pressure is observed at 225 °C, although large (20%) nonlocal strains appear at 125 °C. The elevated-temperature mechanical performance is limited by cracks that initiate on planes of greatest shear under the indenter.

Introduction

Nanoporous materials are of interest because their high surface areas can provide enhanced properties benefiting a wide range of technologies. Of particular interest in this study is the fact that the mechanical properties of such materials exhibit length scale effects [1, 2, 3]. In nanoporous gold, stresses approaching the theoretical shear strength of the material (an upper bound of $\tau = \mu/10$, where μ is the shear modulus) have been reported as the ligament diameter decreases below 100 nm [2]. In addition, the behavior of porous materials scales according to relative density [4], grain size [1], and representative volume [5], allowing for many degrees of freedom in material design.

Nanoporous metals made by dealloying processes have a random arrangement of ligaments and typically possess polycrystalline microstructures and combine the effects of small grain size with the open-pore structure. Open-cell structures made with a number of pure metals, such as Au [1, 2, 5, 6, 7], Cu [8], and W [3] can exhibit very high ligament strengths. The ligament strengths are estimated by inverting property

scaling laws [2]. Nanoporous tungsten made by high-pressure torsion followed by dealloying showed high strength of 5.3 GPa even at a relative density of 65%, corresponding to ligament yield stresses of 2.04 GPa [3]. Meanwhile, 36% dense nanoporous gold with 15 nm thick ligaments shows ligament yield stresses of 1.5 GPa, which is an order of magnitude larger than the yield stresses found in fully dense gold columns [9]. Despite their high ligament strengths, the moderately high relative density in materials produced by dealloying limits their potential as ultra-lightweight materials.

One approach to obtain more periodic structures with low relative density (high porosity) involves colloidal crystal templating to obtain three-dimensionally ordered macroporous (3DOM) materials. Alternatively referred to as inverse opals, 3DOM materials are a type of open-cell material featuring a highly ordered lattice of solid material surrounding interconnected macropores. These feature sizes can be controlled in the range from 50 nm to several micrometers [10]. Moreover, the densities of 3DOM materials can be reduced into the

📘 Journal of Materials Research 🔳 Volume 35 🔳 Issue 19 🖿 Oct 14, 2020 📕 www.mrs.org/jmr

¹Department of Chemical Engineering and Materials Science, University of Minnesota, Minneapolis, Minnesota 55455, USA

²Department of Chemistry, University of Minnesota, Minneapolis, Minnesota 55455, USA

³George W. Woodruff School of Mechanical Engineering, Georgia Institute of Technology, Atlanta, Georgia 30332, USA

^{a)}Address all correspondence to these authors. e-mail: a-stein@umn.edu

b)e-mail: mara@umn.edu

c)These authors contributed equally to this work.



single-digit percentages relative to those of the bulk material [11]. Additional flexibility exists to produce nanoporous thin films and to employ a wide variety of materials (e.g., 3DOM materials have been generated from C [12], V_2O_5 [13], SiO_2 [14, 15], W and W-Mo [16, 17, 18], TiO_2 [11, 19], Ni [20, 21], Cu [22, 23]). These geometries and chemistries are not all readily produced with electrochemical dealloying processes.

3DOM materials possess a small representative volume element [14], implying high periodicity and regularity in mechanical response that in turn simplifies the required data analysis protocols. Although derived for ideal open-cell foams that possess uniform ligaments, Gibson and Ashby open-cell foam models [4] may be applied in some 3DOM materials with a relative density less than 0.3 [4]. Modifications have been made to the scaling inherent to the Gibson–Ashby approach to incorporate other effects, such as those of grain size, characterized by the Hall–Petch relation [1].

The 3DOM structure enables the study of thermally activated, dislocation-mediated deformation processes at small length scales. Some of the materials that have been synthesized in the 3DOM structure do not typically deform via thermally activated mechanisms. These include face-centered cubic (FCC) metals [20, 21, 22, 23], which deform by dislocationmediated processes on close-packed planes and directions, and ceramics [11, 14, 15, 19], which demonstrate limited plasticity at experimentally accessible temperatures. In contrast, body-centered cubic (BCC) metals are known to possess highly temperature-dependent mechanical properties due to increasing numbers of active slip systems ({110},{112}, and {123}) at increasing temperatures [24]. Therefore, a 3DOM structure comprised of BCC metal provides an excellent test bed for studying the effects of increasing slip activity on the overall deformability of a porous nanostructured material. The mechanical properties of a BCC metal are most drastically affected in the region around the brittle-ductile transition (BDT). Many BCC metals have BDT temperatures (BDTTs) around or below room temperature [25-27]. In addition, the BDT is an important consideration for structural materials; neglecting the BDT can have disastrous effects, such as the famous catastrophic hull failures of steel Liberty Ships during World War II [28]. Tungsten is an elastically isotropic, highstrength BCC metal considered for replacements for depleted uranium projectiles for tanks [29] and for divertors in Tokamak-type fusion reactors [30] and possesses a relatively accessible BDTT of around 400 K [31], making it an ideal material for studying the effects of increasing plasticity at small length scales. Synthesis of the 3DOM material as detailed here results in a nanocrystalline microstructure within the ligaments. Given that dense nanocrystalline tungsten thin films exhibit hardness values over 10 GPa (corresponding to a yield strength of approximately 3.4-5 GPa) [3, 32], it is

postulated that the nanocrystalline microstructure in 3DOM tungsten could enable exceptional yield strengths across a range of temperatures.

This article presents the mechanical behavior of 3DOM W (successfully synthesized as in earlier works [16, 17, 18]) across the BDT to assess the effects of increasing plasticity on the mechanical behavior of BCC metals in the 3DOM structure.

Results and discussion

Synthesis of PMMA templates and 3DOM W materials

To fabricate 3DOM W materials, two types of poly(methyl methacrylate) (PMMA) colloidal crystal templates were used. One was prepared through gravity sedimentation of PMMA spheres from its colloidal suspension [33]. The other type was obtained through convective self-assembly of PMMA spheres onto silicon wafers [34]. The sedimentation method produced PMMA monoliths with sizes up to centimeters (monolithic PMMA template). The convective self-assembly method produced PMMA colloidal crystals in the thin-film form (PMMA film template). The film template had fewer defects and cracks than the monolithic PMMA templates. However, in this method, the tensile forces generated during water evaporation caused longitudinal cracks in the PMMA film. In addition, transverse cracks occurred at the boundaries of wet and dry regimes as the water evaporated [35, 36, 37]. Therefore, the PMMA films produced by convective selfassembly formed strips with lengths around 0.5 cm, widths around 0.2 cm, and thicknesses less than 50 µm (Fig. 1).

3DOM W was synthesized through the infiltration of acetylated peroxotungstic acid (APTA) as a tungsten precursor into PMMA colloidal crystal templates followed by reductive heat treatment in the H₂ atmosphere. Either 3DOM W monoliths or 3DOM W films were obtained using the corresponding PMMA template (Fig. 1 and Supplementary Fig. S1). Dwelling at 310 °C helped with the removal of the PMMA templates [38]. Further heating in the H₂ atmosphere enabled the formation of W via reduction of the WO₃ generated from the condensation of APTA. XRD patterns of both the 3DOM W film and monolithic 3DOM W indicated that the material contained α-tungsten (BCC) as its only crystalline phase (Fig. 2).

Extensive volume shrinkage was observed during the processing of 3DOM W, because the majority of the APTA precursor consisted of solvent (water and methanol), which left the system during the heat treatment. To increase the fraction of the APTA in the PMMA template and reduce the occurrence of voids, multiple cycles of APTA infiltration and drying were performed. For monolithic 3DOM W (synthesized from the monolithic PMMA template), multiple infiltrations increased the uptake of APTA molecules and resulted in larger



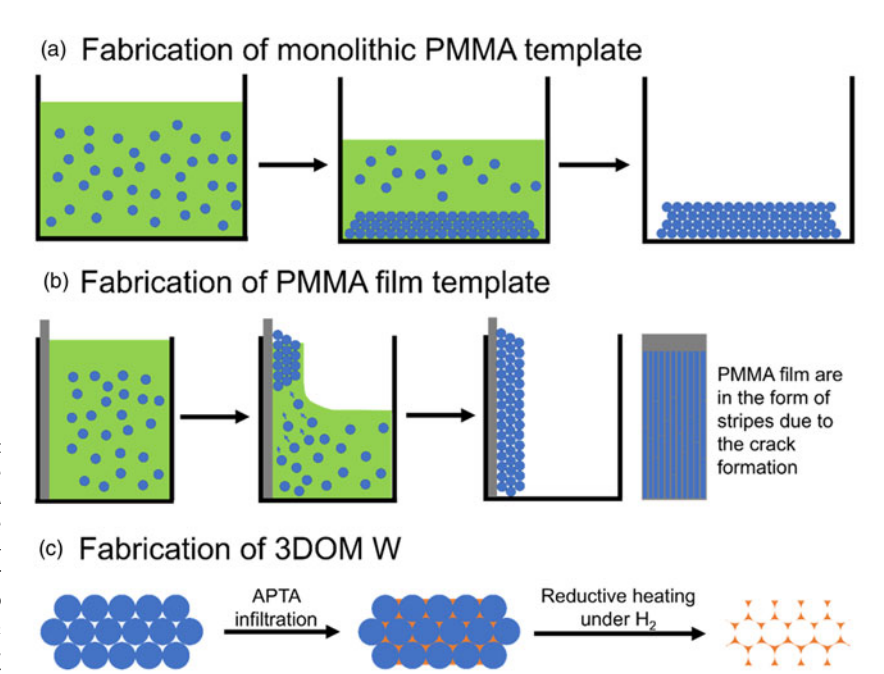


Figure 1: Schematic showing the major synthetic processes. (a) Monolithic PMMA templates were fabricated using gravity sedimentation. (b) PMMA film templates were fabricated using convective self-assembly. (c) In both cases, the PMMA templates were infiltrated with a tungsten precursor solution, and the composite was converted to 3DOM W through reductive heating under H₂ (2 °C/min to 310 °C, remaining at 310 °C for 2 h, then 5 °C/min to 800 °C, remaining at 800 °C for 1 h).

regions of well-defined 3DOM structure (Supplementary Figs. S2 and S3). However, for more than three infiltrations, the monolithic PMMA templates were inclined to crumble into smaller pieces. For the synthesis of 3DOM W films (from PMMA film templates), multiple infiltrations generated a tungsten overlayer resulting from excess APTA precursor (Supplementary Fig. S4). Therefore, monolithic 3DOM W prepared by triple infiltration and 3DOM W film prepared by a single infiltration were employed for the subsequent studies.

Compared to the monolithic 3DOM W, the 3DOM W films exhibited much larger ordered domains (Fig. 3), making

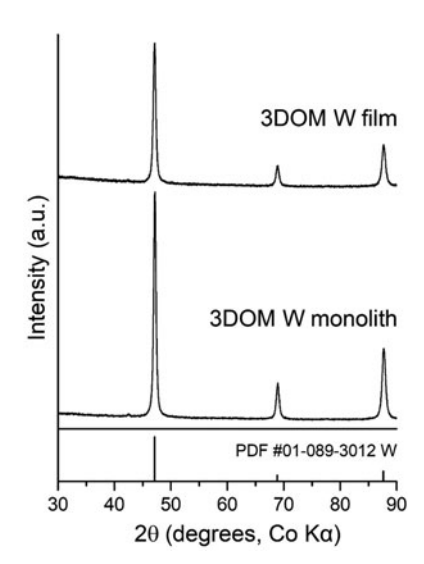


Figure 2: XRD patterns of 3DOM W monolith and film materials. The reference W pattern corresponds to α -tungsten with BCC crystal structure.

them suitable to study a less defective microstructure via frustum indentation, as described in Sec. II.B. The different degrees of order in the 3DOM structures were attributed to the different preparation methods of the PMMA templates. The convective self-assembly method can generate much thinner layers of packed PMMA spheres with uniform thickness compared to the sedimentation method [34, 35]. The thinner PMMA template contains fewer mispacked PMMA spheres, and it is more controllable during the infiltration of precursor, which avoids over- or insufficient infiltration. However, because the PMMA film templates were already thin and had small, continuous domains, the resulting 3DOM W films were even smaller pieces with lateral dimensions in the range of 50-200 µm, thicknesses between 5 and 20 µm, and ligament widths of 35-40 nm (Fig. 4). The thickness of the 3DOM W films was not suitable for the milling of micropillars of sufficient size to ensure a large enough representative volume. The dimensions of monolithic 3DOM W pieces make them suitable for large micropillars, as well as other experiments dealing with larger-scale measurements. The pore size was kept constant in this study for the films and monoliths. It is expected that pore size may influence the mechanical behavior of these materials, and such effects will be studied in future research.

Frustum indentation of 3DOM W

Frames from the failure point of the frustum indentation at 30 °C, 125 °C, and 225 °C are shown in Figs. 5(a)–5(c), respectively. Fig. 5(a) shows that at 30 °C, the indenter tip plunges into 3DOM W. Strain is localized directly under the indenter



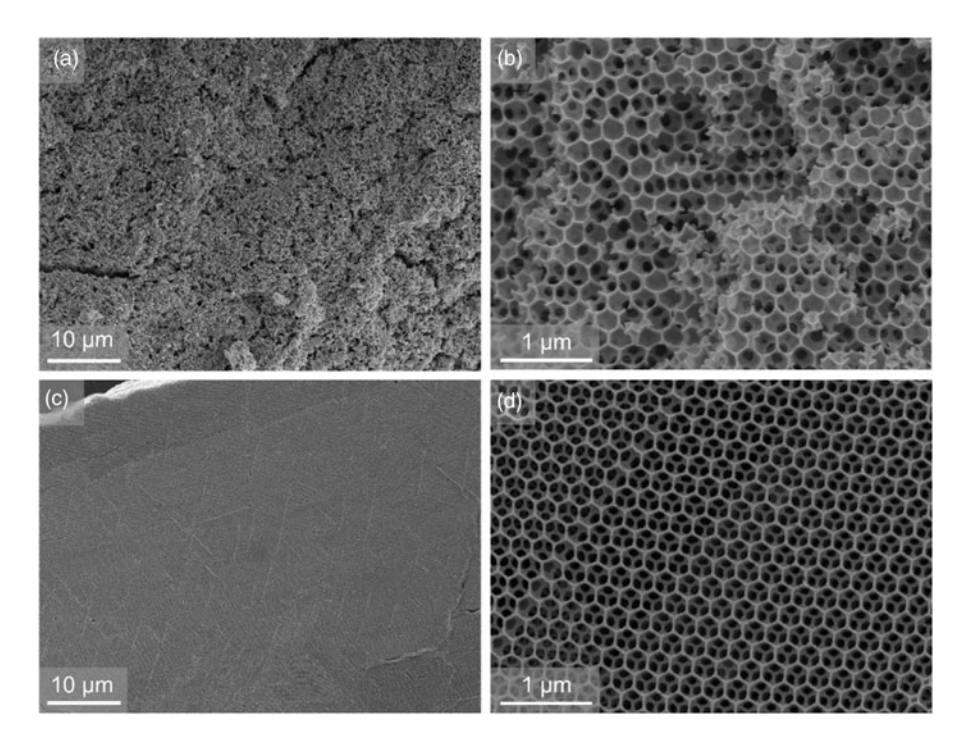


Figure 3: (a, b) SEM images with different magnification of a 3DOM W monolith and (c, d) a 3DOM W film. The 3DOM W film contained larger regions of well-defined and ordered structure.

tip and failure appears to occur on the same length scale as the 3DOM unit cell. Conversely, at both 125 °C [Fig. 5(b)] and 225 °C [Fig. 5(c)], failure occurs on a more global scale with delocalized strains appearing in a larger volume. In this manner, failure occurs via the formation and propagation of cracks that remove larger volumes comprising hundreds of unit cells of material from the bulk.

Figs. 5(d)–5(f) show the vertical (ϵ_{yy}) Eulerian strain maps calculated using the Ncorr algorithm at the time of failure. It is clear from Fig. 5(d) that nearly all strain is localized in the vicinity of the indenter tip; as noted above, this indicates that there is a minimal stress redistribution in 3DOM W at 30 °C. On the other hand, strain fields emanating from the indenter tip can be seen in both the 125 and 225 °C cases, indicating some delocalization of stress to surrounding ligaments.

Images of the deformed area after indentation are shown in Figs. 5(g)–5(i). At 30 °C, it is apparent that the material ultimately conformed to the shape of the indenter tip during the deformation process. Here, the deformation is contained within a region close to the indenter. At higher temperatures, from Fig. 5, the strain field underneath the indenter becomes more distributed, possibly indicating a change in the plastic Poisson's ratio. This behavior is distinctly different from what is seen at higher temperatures in Figs. 5(h) and (i), which show that large pieces of material have sheared off from the bulk structure.

The rotation of the sample with respect to the electron beam makes it difficult to directly compare the shape of the strain field underneath the indenter tip for each sample. Instead, profile traces along the Eulerian strain map at

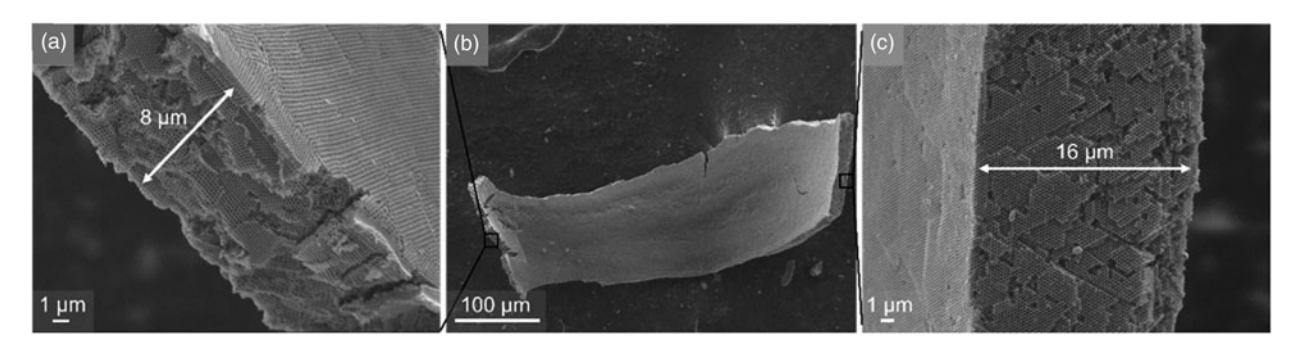


Figure 4: SEM images of a 3DOM W film piece. The lateral dimensions of this piece were around 100 μm and 390 μm. The thickness varied across the piece from 8 μm on the left to 16 μm on the right. Most 3DOM W film pieces had lateral dimensions ranging between 50 and 200 μm.



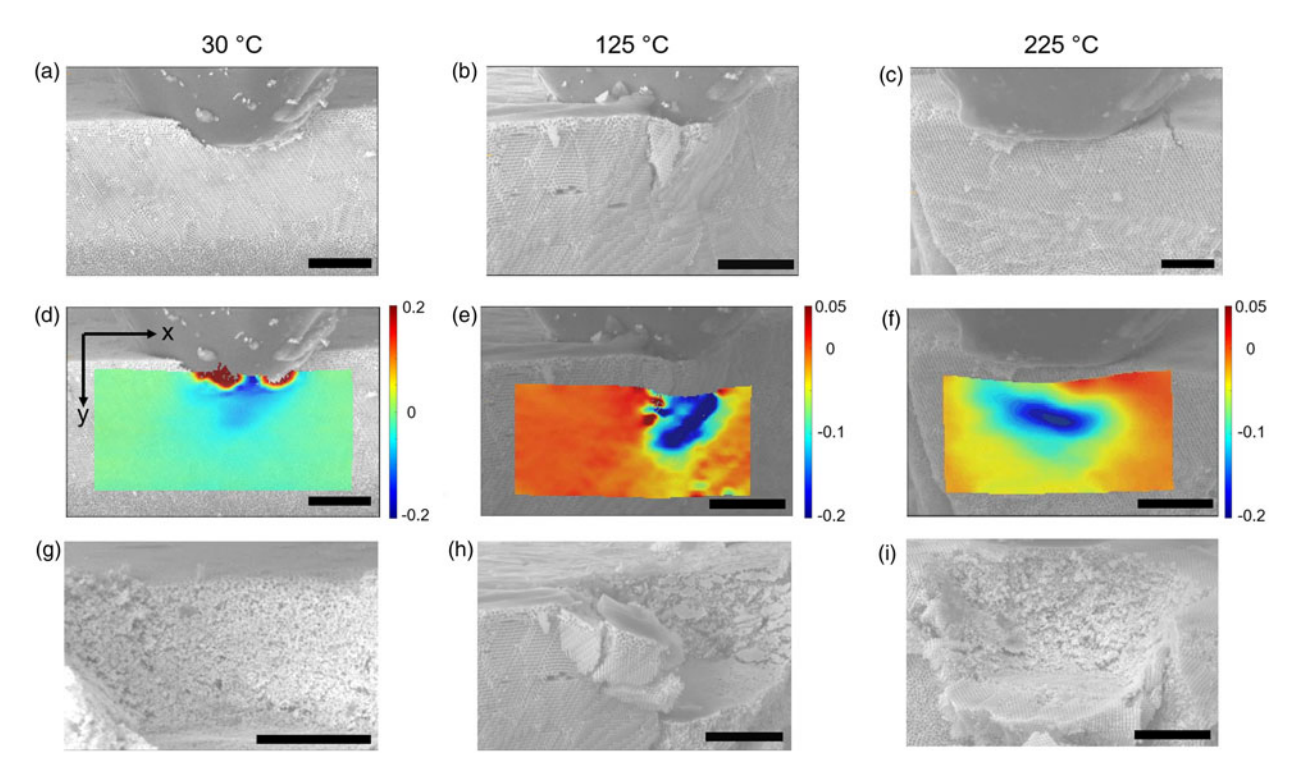


Figure 5: Images from *in situ* frustum compression of a 3DOM W film. Scale bar indicates 5 μ m. (a–c) Images from compression at which failure occurs, i.e., when a major crack can be seen in the structure. (d–f) Eulerian strains in the vertical direction (ϵ_{yy}) at the point just before a major crack is apparent in the 3DOM structure. (g–i) Morphology of residual indent after frustum indentation.

equivalent positions with respect to the indenter axis (along the centerline) (Fig. 6) are used to provide a more representative comparison of the strain distribution underneath the center of the indenter. At 30 °C, the maximum compressive strain along the centerline of the indenter is approximately 0.024. In contrast, maximum compressive strains are nearly an order of magnitude higher at both 125 °C (0.25) and 225 °C (0.21), indicating a large increase in deformability between 30 and 125 °C. This increase in ductility can be attributed to an increase in plasticity, possibly caused by the activation of additional slip systems over those active at 30 °C [24].

Analysis of the contact pressure as a function of the normalized displacement [Fig. 7(a)] enables the further quantitative comparison of the deformation behavior at 30, 125, and 225 °C. The curves shown in Fig. 7(a) were selected to be representative due to the best contact conditions at the start of the experiment, i.e., when the indenter tip and sample were closest to parallel such that the contact was most uniform at the beginning of the experiment. At 30 °C, there is a very short initial loading region (h/a~0.05–0.09) before the mean contact pressure continues to increase linearly. This behavior is described as an initial loading region because the exact deformation processes during this regime are not currently known. The increase in mean contact pressure is likely a result of the densification of the material underneath the indenter tip at increased displacements. The degree to which this occurs is heightened

after $h/a\sim 1$, where there are two important effects: the increased contact area from the 60° angle of the cone, as well as the densified material underneath the indenter tip.

Increasing the temperature from 30 °C changes the deformation behavior significantly. As noted earlier, the material does not deform by purely brittle fracture above 30 °C. This can be seen by a longer initial loading region at 125 °C. However, at 125 °C, the mean contact pressure increases along this initial loading region curve until higher strains are reached before the slope begins to decrease. The point of slope decrease coincides with a large crack forming in the material, as can be seen in Fig. 5(b). Increasing the temperature further to 225 °C again distinctly changes the behavior; the initial loading region regime has a distinctly different slope from the lower temperatures, indicating that a different deformation mechanism is likely occurring. One of the most important features exhibited at 225 °C is that the slope of the contact pressure-strain curve begins to change at approximately 1800 MPa, before a crack is seen in the material, unlike in the lower temperature cases, where a slope change coincides with a crack in the material. This slope change prior to largescale fracture is thought to be the onset of large-scale plasticity which is not seen in the lower temperature cases.

Since the stress state changes significantly after a large-scale fracture has occurred, it is reasonable to analyze only the pre-fracture behaviors, as seen in Fig. 7(b). The nondimensional



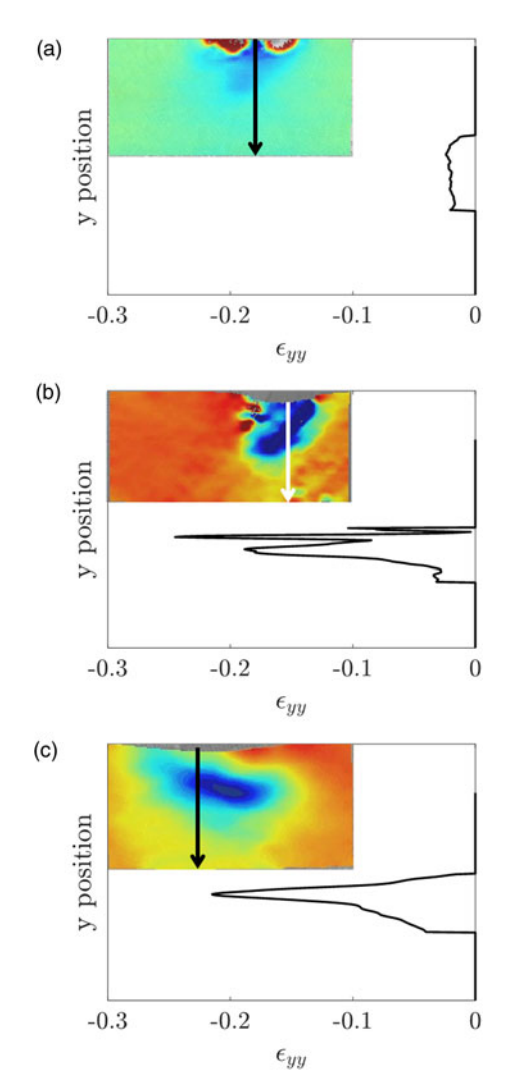


Figure 6: Profile of Eulerian strains from DIC analyses at (a) 30 °C; (b) 125 °C; (c) 225 °C.

displacement at failure is difficult to characterize at 30 °C because a macroscopic crack does not form. From the comparison of these curves, one can immediately notice that the nondimensional displacements at macroscopic failure are relatively similar in the elevated temperature experiments and much higher than at 30 °C. This may be due to the large stress concentration around the edges of a flat punch indenter. However, it is also obvious that the contact stresses that the material can sustain at 225 °C are significantly higher than at the lower temperatures. The areas underneath these curves are directly related to the amount of energy absorbed by the material during the deformation process. A comparison indicates that approximately six times more mechanical energy is absorbed by the 3DOM W structure at 125 °C compared to at 30 °C, and approximately 18 times more at 225 °C, likely due to an increase in the plasticity of the ligaments of the structure.

To further illustrate this point, it is important to look at the mean contact pressure at the time of failure, which can be seen

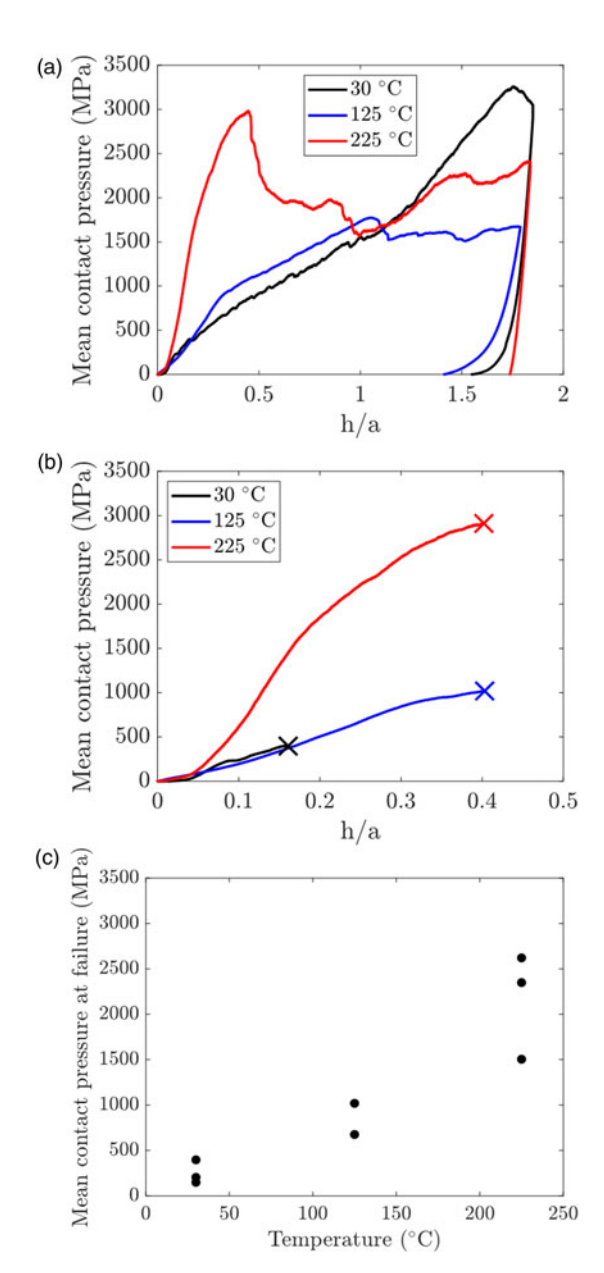


Figure 7: Quantification of mean contact pressures from *in situ* frustum indentation. (a) Mean contact pressure for selected tests as a function of temperature. Tests were selected based on the flattest indenter-sample contact. (b) A focused view of the initial loading of the tests in (a) up to the point of failure, indicated by the 'x' symbol. (c) Mean contact pressure at the point of failure, i.e., when a crack formed in the material, as a function of deformation temperature.

plotted as a function of temperature in Fig. 7(c). At 30 °C, the mean contact pressure at the time of failure is very low; the W ligaments appear to fracture at relatively low stresses in the absence of large-scale plasticity. In contrast, the stresses at failure are nearly a factor of 2 higher at 125 °C and nearly an order of magnitude higher at 225 °C. The higher sustained contact pressure at failure is likely due to the delocalization of stress to other ligaments before widespread plasticity rather than a fracture of ligaments.



BCC materials like tungsten are known to have multiple active slip planes at higher temperatures, namely {110}, {112}, and {123}-type planes [30]. At 30 °C, only a subset of these active slip planes may be energetically favorable for slip. Because the ligament diameter is on the order of 40 nm, a flaw on the order of a few nm may have a large enough stress concentration for the ligament to undergo brittle fracture in the absence of plasticity. At 30 °C, when fewer slip systems are active, and in a small volume of material, where fewer dislocation sources may exist, it is likely that fracture is preferred over large-scale plastic deformation. However, as the temperature is increased, the number of energetically favorable slip systems may be significantly higher, allowing for larger-scale plasticity.

The similarities in the initial loading region slopes of the 30 and 125 °C experiments could indicate that similar behavior is occurring initially. However, as the indenter continues to press into the material, the stresses underneath the indenter continue to rise. At 30 °C, plastic deformation is limited because it is easier to deform the material by ligament fracture than to nucleate dislocations in the ligaments. At 125 °C, the behavior is fracture-dominated at lower contact pressures; at higher contact pressures, there is enough stress to nucleate new dislocations from the sources which are likely to be more active at the higher temperature. Therefore, the contact pressure continues to increase because ligaments are plastically deforming rather than breaking, allowing for mixed behavior between fracture and plasticity.

The behavior at 225 °C is distinctly different. The slope of the initial loading region is significantly higher than what is seen at 30 °C and 125 °C. It is likely that this is due to reduced brittle fracture in the ligaments. At this temperature, more slip systems are energetically favorable; thus, dislocation sources are more likely to be favorably oriented for nucleation at lower stresses. These dislocation sources, therefore, can emit dislocations at the lower stresses seen at lower mean contact pressures. Thus, ligaments plastically deform prior to rupture rather than undergoing brittle fracture, resulting in a structure that appears macroscopically stiffer.

Through these experiments, it is possible to infer that the material is undergoing a BDT with increasing temperature. At 30 °C, the local behavior under the indenter tip appears to be mostly, if not entirely, brittle, whereas significant plasticity is evident at 225 °C. As these were not fracture experiments and they were performed with relatively large temperature steps, it is difficult to identify a distinct BDT temperature (BDTT). The BDT is thought to be controlled by dislocation mobility [31], particularly screw dislocations in tungsten. A BDT is therefore thought to correlate with the increase in plasticity that is observed here. However, it is evident that a BDT begins somewhere below 125 °C, where in bulk W, plasticity begins to be enhanced. This is in relative agreement with the

literature regarding the BDTT of bulk single crystals of tungsten; Gumbsch et al. [31] found the BDTT of tungsten single crystals to depend on both crack plane and crack front direction, ranging from 370–470 K. The BDT also is not a sharp transition, as shown by both Gumbsch for macroscale crystal fracture and Ast et al. [39] for fracture of microcantilevers oriented for fracture along the {100}<010> crack system. In addition, 3DOM W is polycrystalline; some averaging of the BDTT across crack systems is to be expected. Thus, the presence of a range of temperatures for the BDTT is expected and in agreement with the literature.

Micropillar compression of 3DOM W

A frame from the failure of a micropillar of monolithic 3DOM W can be seen in Fig. 8(a). In the frame, it is clear that there are extended voids within the structure of the 3DOM W, as well as ordering that is not as perfect as the ordering seen in Fig. 3. As shown in Fig. 8(a), the failure point in the micropillar, unsurprisingly, occurs at a large concentration of these voids.

Strain maps of the micropillar prior to the failure described above results in the frame shown in Fig. 8(b). The alternating bands of strain are collapse (compaction) bands that are characteristic of deformation of low relative density porous solids [40, 41, 42]. As such, an Ashby-type model [4] for foams is applicable to the structure. Because the constants for such a model should be functions only of the structure [43], the model seems applicable to the 3DOM W structure in this study. The model employed here was developed by Pikul et al. using finite element simulations of Ni inverse opals assuming isotropic elasticity [20]:

$$\sigma^* = 0.78\sigma_y \left(\frac{\rho^*}{\rho_s}\right)^{1.52},$$

where σ^* is the measured yield strength of the pillar, σ_v is the yield strength in the ligament, and ρ^*/ρ_s is the relative density, i.e., the density of the 3DOM material divided by the density of bulk, non-porous tungsten. Using a relative density of 5% and a pillar yield stress of 50 MPa, the ligament yield stress is calculated to be 6.1 GPa. In single-crystalline tungsten pillars compressed along the [001] direction, yield stresses of 3.5 GPa have been reported in 200 nm diameter pillars [44]. Yield stresses of 2 GPa were found in 200 nm diameter single crystalline pillars oriented along the [235] direction for single slip [45], indicating plastic anisotropy. However, in 200 nm diameter pillars of either orientation, the stress-strain curves are not smooth; the authors posit one possible explanation of dislocation nucleation-mediated deformation behavior in line with the observations seen in their stress-strain curves. In polycrystalline 3DOM W, where ligament diameters are significantly smaller than 200 nm, one would expect that the deformation continues



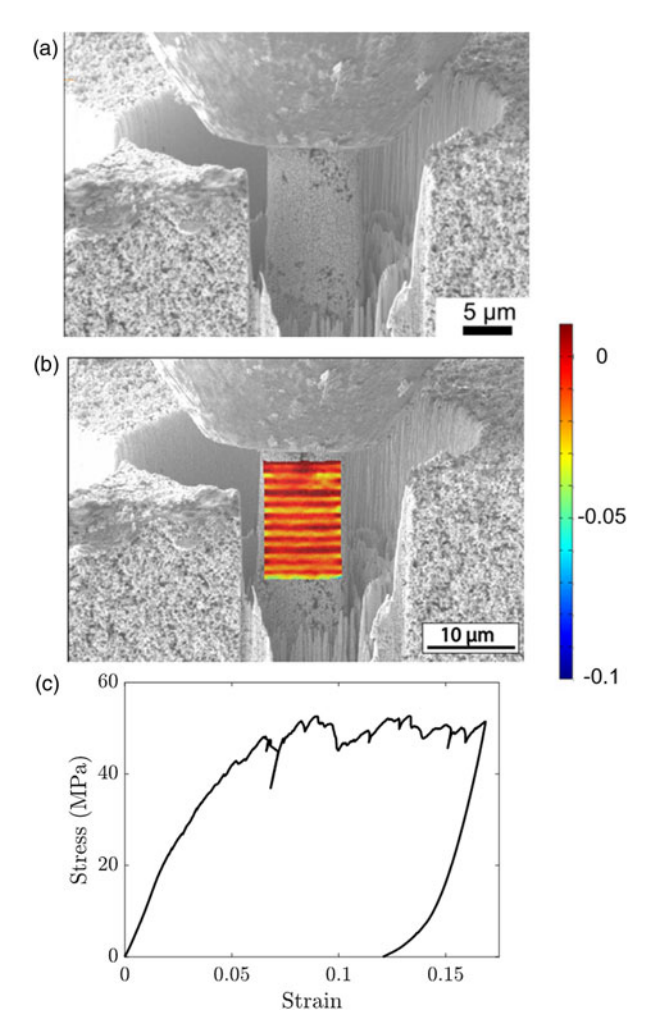


Figure 8: Micropillar compression of monolithic 3DOM W. (a) Failure of pillar due to buckling caused by voids at the bottom of the pillar; (b) DIC Eulerian strain map (ϵ_{yy}) of pillar during compression showing compaction bands; (c) Engineering stress-strain curve for the compression of the micropillar in (a).

to be dislocation nucleation-mediated and that the ligament yield stresses further increase due to the lack of active dislocation nucleation sites.

Conclusion

3DOM materials possess two important features that bolster mechanical performance: small ligament diameters which exploit material size effects and lattice periodicity. Studied here are the mechanical behaviors of ordered metallic tungsten porous solids across the BDT. Micropillar compression tests at 30 °C reveal structural failure at a contact pressure of around 50 MPa, and utilizing a Gibson-Ashby model from the literature [20] reveals ligament yield strengths on the order of 6.1 GPa. In situ frustum indentation of 3DOM W shows low contact pressures before failure at 30 °C, but nearly an order of magnitude increase in sustained contact pressure at 225 °C. In addition, strain maps during frustum indentation

reveal the local strains underneath the indenter tip. Compressive strains on the order of 2% are seen at 30 °C under the center of the indenter tip, whereas compressive strains on the order of 20% are seen at both 125 and 225 °C. Although the sustained contact pressures are not nearly as high at 125 °C as at 225 °C, it is clear from the strain maps that there is a significant degree of nonlocal deformation in the structure. The plastic deformation of the 3DOM structure at 225 °C allowed for nearly 18 times mechanical energy absorption compared to 30 °C. Finally, this model system has also shown a temperature-dependent enhancement in properties that may be exploited for engineering applications in a low-density structure with small ligament lengths.

Methods

Materials

The following chemicals were used as-received: 2,2'-azobis (2-methylpropionamidine) (99+%), methyl methacrylate (99.9%), tungsten monocrystalline powder (99.9+%, 0.6-1 micrometer sizes) from Aldrich Chemical Company; glacial acetic acid (ACS grade) from VWR International; hydrogen peroxide (certified ACS, 30%) from Fischer Chemical; methanol (ACS reagent, >99.8%) from Sigma-Aldrich; hydrogen gas (industrial grade) and argon gas (UHP/zero gas) from Matheson.

Synthesis

Synthesis of the PMMA colloidal crystal templates

PMMA spheres with an average diameter of 397 ± 4 nm were synthesized by emulsifier-free emulsion polymerization following established methods [33]. These were assembled either into monolithic pieces by gravity sedimentation or thin films by convective self-assembly. For gravity sedimentation, a 15 wt% aqueous dispersion of the PMMA spheres was placed in a crystallization dish and allowed to settle for several weeks. Monolithic PMMA colloidal crystals gradually formed at the bottom of the crystallization dish as the spheres settled and the dispersion dried. For convective self-assembly, a silicon wafer with dimensions of 1.5 cm × 3.0 cm was placed vertically into a 10 mL beaker [34, 46, 47]. A 1 wt% aqueous PMMA sphere dispersion was then added into the beaker, partially immersing the silicon wafers. The bottom of the beaker was heated to 65 °C. A PMMA colloidal crystal film formed on the silicon wafers as the water evaporated. Typically, a 2-cm long assembly formed in 3 h.

Synthesis of 3DOM W

Two types of 3DOM W materials were synthesized. One was denoted as monolithic 3DOM W, prepared from monolithic



PMMA templates. The other one was denoted as 3DOM W film, prepared from PMMA thin films. The synthesis of monolithic 3DOM W was carried out following a previously reported method, using APTA as the tungsten precursor [17]. Details are provided in the Supporting Information. 3DOM W films were prepared by infiltrating the PMMA thin film templates with APTA solution and then heating the material under H2 to remove the PMMA template and reduce the precursor to metallic tungsten. Detailed procedures are: using a syringe, a 1 M solution of APTA in a mixture of water and methanol (4:1 in volume) was injected to one end of the PMMA colloidal film template on the Si wafer. The precursor gradually diffused to infiltrate the whole template. Any excess precursor solution was wiped off with Kimtech wipes and the film was allowed to dry in air for 12 h. Then, the infiltrated PMMA colloidal template was processed by heat treatment under H₂ at 1 atm (2 °C/ min to 310 °C, remaining at 310 °C for 2 h, then 5 °C/min to 800 °C, remaining at 800 °C for 1 h). The resulting 3DOM W pieces had lateral dimensions ranging from 50 to 200 µm, with thicknesses between 5 and 20 µm, depending on the sample.

Characterization

Powder X-ray diffraction patterns were collected using a PANalytical X'Pert Pro diffractometer. The X-rays were generated with a Co anode (K α radiation, λ = 1.789 Å) which was operated at 45 kV accelerating voltage, 40 mA emission current. Thermogravimetric analysis (TGA) was performed on a Netzsch STA 409 instrument. Samples were heated in air at a ramp rate of 5 °C/min. Scanning electron microscopy (SEM) was performed on a JEOL-6500 field-emission scanning electron microscope with an accelerating voltage of 5.0 kV. All samples were coated with a 50 Å platinum film prior to SEM imaging.

Pillars with a diameter of 10 μ m and an aspect ratio of approximately 2 were machined using an annular milling procedure on an FEI Helios G4 UX dual-beam FIB/SEM. All cuts were performed with an accelerating voltage of 30 kV and an ion current of 9.1 nA. Initial annuli with an inner diameter of 22 μ m were cut prior to decreasing the annuli size to 13 μ m. Final polishing cuts to reduce taper and achieve final diameter were performed at ion currents of 1.2 nA.

Micromechanical testing

Frustum testing

Thin films of 3DOM W were mounted with M-Bond 610 adhesive (Vishay Micro-Measurements, Malvern, PA) to the silicon wafer for frustum indentation. To minimize the amount of adhesive absorbed by the material, the substrate was heated to \sim 150 °

C prior to the application of the adhesive and allowed to partially cure prior to the addition of 3DOM W pieces. The adhesive was then cured at 175 °C for 1 h. The samples were compressed *in situ* in an FEI Helios G4 UX dual-beam FIB/SEM using a Hysitron PI88 Picoindenter (Bruker Nanosurfaces, Minneapolis, MN) equipped with an xR High Load Transducer and a 10 µm diameter diamond flat punch tip with a 60° cone angle. The films were compressed in displacement control at 30, 125, and 225 °C with a displacement rate of 20 nm/s. Although annealing in tungsten is not expected at these temperatures, higher temperature experiments were performed first to minimize any microstructural differences between temperatures. Frustum indentation was performed on the edges of film 3DOM pieces to probe the mechanical response in a more idealized, less defective structure.

The mean contact pressures were quantified using the method of Liu et al. [8]. The mean contact pressure is the load divided by the contact area of the indenter. In cases where the indenter tip overhung the edge of the sample, the contact area was calculated by [8]:

$$A_c = \frac{a^2}{2(O - \sin(O))}, \quad 0 < x < a,$$

where $Q = 2\cos^{-1}(|x-1|)$, a is the indenter contact radius, and x is the fractional indenter overhang. An overhang of x = 1 corresponds to half of the indenter being in contact with the sample and half overhanging, whereas x = 0 is full contact such that $A_c = \pi a^2$. In this study, the dimensionless overhang ranged from 0 to $\frac{3}{4}$; the majority of tests were performed with $x \le \frac{1}{2}$. In addition, the displacement is normalized by the contact radius of the indenter tip to achieve a dimensionless displacement.

Micropillar compression

Monolithic 3DOM W pieces were mounted to a silicon wafer with PELCO high-temperature carbon paste (Ted Pella, Redding, CA). A thin layer of paste was spread on the wafer prior to the addition of 3DOM W pieces. The paste was cured at 90 °C for 2 h, then 260 °C for 2 h. Samples were compressed in situ in an FEI Helios G4 UX dual-beam FIB/SEM using a Hysitron PI88 Picoindenter (Bruker Nanosurfaces, Minneapolis, MN) equipped with an xR Low Load Transducer and a 20 µm diameter diamond flat punch tip with 60° cone angle. Pillars were compressed in displacement control at engineering strain rates of approximately 5 × 10⁻⁴ s⁻¹. Stresses were calculated by dividing the load by the cross-sectional area of the top of the pillar. Monolithic 3DOM W pieces were used for pillar testing to ensure that an appropriate representative volume would be contained within a pillar; the thickness of the 3DOM W films would not allow the formation of pillars with these same dimensions.



In-plane strain maps

SEM images either of the micropillar or the sample edge were further processed using digital image correlation (DIC) to obtain in-plane strain maps. The analysis determined the relative displacements in the deformed specimen based on comparison to reference (undeformed) images. The native features of the 3DOM structure provided sufficient contrast for the DIC algorithm to track points during the deformation process without the need for an applied speckle pattern. Videos recorded during the in situ compression of the 3DOM structure were separated into individual frames. To shorten the processing time, every third frame was used without additional image post-processing. DIC analysis was performed using an open-source analysis algorithm (Ncorr) [48]. The applied subset radius was 150 nm, and the strain radius was 250 nm. This package was used to calculate (i) the horizontal normal strain (ϵ_{xx}) , (ii) the vertical normal strain (ε_{yy}) , and (iii) the in-plane shear strain (ε_{xy}) . Due to the slight variations in the rotation of the sample with respect to the viewing axis, only the vertical normal strains (ε_{yy}) are presented here. The vertical normal strains (ε_{vv}) also provide a useful comparison of strains between frustum and micropillar experiments.

Acknowledgments

This work was supported primarily by the MRSEC Program of the National Science Foundation under Award Number DMR-1420013. The authors would like to thank Erica Lilleodden for helpful discussions related to the analysis of DIC results. The authors would also like to thank Bill Gerberich for discussions and suggestions for future work. Parts of this work were carried out in the Characterization Facility, University of Minnesota, which receives partial support from NSF through the MRSEC program. Additional thanks to Nick Seaton (UMN Characterization Facility) for assistance with SEM and FIB.

Supplementary material

To view supplementary material for this article, please visit https://doi.org/10.1557/jmr.2020.130.

References

- A.M. Hodge, J. Biener, J.R. Hayes, P.M. Bythrow, C.A. Volkert, and A.V. Hamza: Scaling equation for yield strength of nanoporous open-cell foams. *Acta Mater.* 55(4), 1343 (2007).
- C.A. Volkert, E.T. Lilleodden, D. Kramer, and J. Weissmüller: Approaching the theoretical strength in nanoporous Au. *Appl. Phys. Lett.* 89(6), 10 (2006).

- M. Zhao, I. Issa, M.J. Pfeifenberger, M. Wurmshuber, and
 D. Kiener: Tailoring ultra-strong nanocrystalline tungsten nanofoams by reverse phase dissolution. *Acta Mater.* 182, 215 (2020).
- **4. L.J. Gibson and M.F. Ashby**: *Cellular Solids*: *Structure and Properties* (Cambridge University Press, Cambridge, 1988).
- K. Hu, M. Ziehmer, K. Wang, and E.T. Lilleodden: Nanoporous gold: 3D structural analyses of representative volumes and their implications on scaling relations of mechanical behaviour. *Philos.* Mag. 96(32–34), 3322 (2016).
- H.J. Jin, L. Kurmanaeva, J. Schmauch, H. Rösner, Y. Ivanisenko, and J. Weissmüller: Deforming nanoporous metal: Role of lattice coherency. *Acta Mater.* 57(9), 2665 (2009).
- M. Caro, W.M. Mook, E.G. Fu, Y.Q. Wang, C. Sheehan, E. Martinez, J.K. Baldwin, and A. Caro: Radiation induced effects on mechanical properties of nanoporous gold foams. *Appl. Phys. Lett.* 104(23) (2014).
- R. Liu, S. Pathak, W.M. Mook, J.K. Baldwin, N.A. Mara, and A. Antoniou: In situ frustum indentation of nanoporous copper thin films. *Int. J. Plast.* 98, 139 (2017).
- C.A. Volkert and E.T. Lilleodden: Size effects in the deformation of sub-micron Au columns. *Philos. Mag.* 86(33-35 SPEC. ISSUE), 5567 (2006).
- A. Stein, B.E. Wilson, and S.G. Rudisill: Design and functionality of colloidal-crystal-templated materials – chemical applications of inverse opals. Chem. Soc. Rev. 42, 2763 (2013).
- R.C. Schroden, M. Al-Daous, C.F. Blanford, and A. Stein: Optical properties of inverse opal photonic crystals. *Chem. Mater*, 14(8), 3305 (2002).
- Z. Wang, F. Li, N.S. Ergang, and A. Stein: Effects of hierarchical architecture on electronic and mechanical properties of nanocast monolithic porous carbons and carbon-carbon nanocomposites. *Chem. Mater.* 18(23), 5543 (2006).
- N.S. Ergang, M.A. Fierke, Z. Wang, W.H. Smyrl, and A. Stein: Fabrication of a fully infiltrated three-dimensional solid-state interpenetrating electrochemical cell. *J. Electrochem. Soc.* 154(12), A1135 (2007).
- 14. J.J. do Rosário, J.B. Berger, E. Lilleodden, R.M. McMeeking, and G.A. Schneider: The stiffness and strength of metamaterials based on the inverse opal architecture. *Extrem. Mech. Lett.* 12, 86 (2017).
- **15.** Y. Toivola, A. Stein, and R.F. Cook: Depth-sensing indentation response of ordered silica foam. *J. Mater. Res.* **19**(01), 260 (2004).
- N.R. Denny, F. Li, D.J. Norris, and A. Stein: In situ high temperature TEM analysis of sintering in nanostructured tungsten and tungsten-molybdenum alloy photonic crystals. *J. Mater. Chem.* 20(8), 1538 (2010).
- N.R. Denny, S. Han, R.T. Turgeon, J.C. Lytle, D.J. Norris, and A. Stein: Synthetic approaches toward tungsten photonic crystals for thermal emission. *Proc. SPIE* 6005(November), 600505 (2005).



- N.R. Denny, S.E. Han, D.J. Norris, and A. Stein: Effects of thermal processes on the structure of monolithic tungsten and tungsten alloy photonic crystals. *Chem. Mater.* 19(18), 4563 (2007).
- M. Curti, G. López Robledo, P.C. dos Santos Claro, J.H. Ubogui, and C.B. Mendive: Characterization of titania inverse opals prepared by two distinct infiltration approaches. *Mater. Res. Bull.* 101 (January), 12 (2018).
- J.H. Pikul, S. Özerinç, B. Liu, R. Zhang, P.V. Braun, V.S. Deshpande, and W.P. King: High strength metallic wood from nanostructured nickel inverse opal materials. Sci. Rep. 9(719), 1 (2019).
- H. Yan, C.F. Blanford, B.T. Holland, M. Parent, W.H. Smyrl, and A. Stein: A chemical synthesis of periodic macroporous NiO and metallic Ni. *Adv. Mater.* 11(12), 1003 (1999).
- Q.N. Pham, M.T. Barako, J. Tice, and Y. Won: Microscale liquid transport in polycrystalline inverse opals across grain boundaries. Sci. Rep. 7(1), 1 (2017).
- 23. C. Zhang, J.W. Palko, M.T. Barako, M. Asheghi, J.G. Santiago, and K.E. Goodson: Enhanced capillary-fed boiling in copper inverse opals via template sintering. Adv. Funct. Mater. 28(41), 1 (2018).
- **24.** C.R. Weinberger, B.L. Boyce, and C.C. Battaile: Slip planes in bcc transition metals. *Int. Mater. Rev.* **58**(5), 296 (2013).
- E.D. Hintsala, C. Teresi, A.J. Wagner, K.A. Mkhoyan, and W.W. Gerberich: Fracture transitions in iron: Strain rate and environmental effects. J. Mater. Res. 29(14), 1513 (2014).
- K. Jatavallabhula and W.W. Gerberich: Fatigue thresholds and ductile-brittle transitions in Ti-30Mo. Fatigue Fract. Eng. Mater. Struct. 4(2), 173 (1981).
- A.S. Wronski, A.C. Chilton, and E.M. Capron: The ductilebrittle transition in polycrystalline molybdenum. *Acta Metall.* 17, 751 (1969).
- 28. M.D. Harris, W.J. Grogg, A. Akoma, B.J. Hayes, R.F. Reidy, E.F. Imhoff, and P.C. Collins: Revisiting (some of) the lasting impacts of the liberty ships via a metallurgical analysis of rivets from the SS "John W. Brown". *Jom* 67(12), 2965 (2015).
- 29. J.P. Bolton and C.R. Foster: Battlefield use of depleted uranium and the health of veterans. J. R. Army Med. Corps. 148(3), 221 (2002).
- **30. R.G. Abernethy**: Predicting the performance of tungsten in a fusion environment: A literature review. *Mater. Sci. Technol.* **33**(4), 388 (2017).
- P. Gumbsch, J. Riedle, A. Hartmaier, and H.F. Fischmeister: Controlling factors for the brittle-to-ductile transition in tungsten single crystals. *Science* 282(5392), 1293 (1998).
- O. El-Atwani, J. Gigax, M. Chancey, J.K. Baldwin, and
 S.A. Maloy: Nanomechanical properties of pristine and heavy ion irradiated nanocrystalline tungsten. Scr. Mater. 166, 159 (2019).
- **33. B.T. Holland, C.F. Blanford, T. Do, and A. Stein**: Synthesis of highly ordered, three-dimensional, macroporous structures of

- amorphous or crystalline inorganic oxides, phosphates, and hybrid composites. *Chem. Mater.* **11**(3), 795 (1999).
- P. Jiang, J.F. Bertone, K.S. Hwang, and V.L. Colvin: Single-crystal colloidal multilayers of controlled thickness. *Chem. Mater.* 11(8), 2132 (1999).
- 35. Y. Suh, Q. Pham, B. Shao, and Y. Won: The control of colloidal grain boundaries through evaporative vertical self-assembly. *Small* 15(12), 1 (2019).
- M.S. Tirumkudulu and W.B. Russel: Cracking in drying latex films. Langmuir 21(11), 4938 (2005).
- K.B. Singh and M.S. Tirumkudulu: Cracking in drying colloidal films. Phys. Rev. Lett. 98(21), 1 (2007).
- 38. S.G. Rudisill, N.M. Hein, D. Terzic, and A. Stein: Controlling microstructural evolution in pechini gels through the interplay between precursor complexation, step-growth polymerization, and template confinement. *Chem. Mater.* 25(5), 745 (2013).
- J. Ast, J.J. Schwiedrzik, J. Wehrs, D. Frey, M.N. Polyakov,
 J. Michler, and X. Maeder: The brittle-ductile transition of tungsten single crystals at the micro-scale. *Mater. Des.* 152, 168 (2018).
- 40. H. Bart-Smith, A.F. Bastawros, D.R. Mumm, A.G. Evans, D.J. Sypeck, and H.N.G. Wadley: Compressive deformation and yielding mechanisms in cellular Al alloys determined using X-ray tomography and surface strain mapping. *Mater. Res. Soc. Symp. –* Proc. 521(10), 71 (1998).
- 41. A.F. Bastawros, H. Bart-Smith, and A.G. Evans: Experimental analysis of deformation mechanisms in a closed-cell aluminum alloy foam. *J. Mech. Phys. Solids* 48(2), 301 (2000).
- K.A. Issen and J.W. Rudnicki: Conditions for compaction bands in porous rock. J. Geophys. Res. Solid Earth 105(B9), 21529 (2000).
- **43. L.R. Meza, S. Das, and J.R. Greer**: Strong, lightweight, and recoverable three-dimensional ceramic nanolattices. *Science* **345** (6202), 1322 (2014).
- A.S. Schneider, D. Kaufmann, B.G. Clark, C.P. Frick,
 P.A. Gruber, R. Monig, O. Kraft, and E. Arzt: Correlation
 between critical temperature and strength of small-scale bcc pillars.
 Phys. Rev. Lett. 103(105501), 105501 (2009).
- 45. A.S. Schneider, C.P. Frick, B.G. Clark, P.A. Gruber, and E. Arzt: Influence of orientation on the size effect in bcc pillars with different critical temperatures. *Mater. Sci. Eng. A* 528(3), 1540 (2011).
- **46.** Y.A. Vlasov, X.Z. Bo, J.C. Sturm, and D.J. Norris: On-chip natural assembly of silicon photonic bandgap crystals. *Nature* **414** (6861), 289 (2001).
- S. Wong, V. Kitaev, and G.A. Ozin: Colloidal crystal films: advances in universality and perfection. J. Am. Chem. Soc. 125(50), 15589 (2003).
- **48. J. Blaber, B. Adair, and A. Antoniou**: Ncorr: Open-source 2D digital image correlation Matlab Software. *Exp. Mech.* **55**(6), 1105 (2015).